ADVANCED INTELLIGENT SYSTEMS
Open Access
www.advintellsyst.com

Machine Learning Based on Digital Image Colorimetry Driven In Situ, Noncontact Plasma Etch Depth Prediction

Minji Kang, Seongho Kim, Eunseo Go, Donghyeon Paek, Geon Lim, Muyoung Kim, Changmin Kim, Soyeun Kim, Sung Kyu Jang, Moon Soo Bak, Min Sup Choi, Woo Seok Kang, Jaehyun Kim, Jaekwang Kim, and Hyeong-U Kim**

This study presents a noncontact, in situ framework for etch depth prediction in plasma etching using machine learning (ML) and digital image colorimetry (DIC). While conventional ex situ methods offer accuracy, they suffer from delays and contamination risks. To overcome these, two approaches are explored. First, etch depth is initially obtained through ellipsometry mapping and used to train an artificial neural network (ANN) based on process parameters (e.g., plasma power, pressure, and gas flow), achieving significantly lower mean squared error (MSE) than a linear baseline. This is extended with a Bayesian neural network (BNN) to capture uncertainty in the predictions. Second, it is demonstrated that red, green, and blue data from DIC alone can effectively predict etch depth without relying on process parameters. Together, these findings establish ML-DIC integration as a real-time, low-cost, and noninvasive alternative for plasma process monitoring.

1. Introduction

Silicon dioxide (SiO_2) and silicon nitride (SiNx) are critical insulating materials in semiconductor devices such as metal-oxide-semiconductor field-effect transistors (MOSFETs),[1–3] dynamic random-access memory (DRAM),[4] and NAND flash memory,[5] valued for their excellent dielectric properties and process compatibility. Insulator thickness directly affects device performance and reliability—for example, gate oxide thickness influences threshold voltage in MOSFETs,[4,6] while dielectric variation in DRAM[7] impacts data retention and leakage. Furthermore, nonuniformity in etch stop layer thickness during etching can result in over-etching or

M. Kang, S. Kim, D. Paek, M. Kim, W. S. Kang, H.-U. Kim
Semiconductor Manufacturing Research Center
Korea Institute of Machinery and Materials (KIMM)
Daejeon 34103, Republic of Korea
E-mail: guddn418@kimm.re.kr

M. Kang, S. Kim, M. S. Choi
Department of Materials Science and Engineering
Chungnam National University (CNU)
Daejeon 34134, Republic of Korea

E. Go
Department of Organic Materials Engineering
Chungnam National University (CNU)
Daejeon 34134, Republic of Korea

G. Lim
Department of Laser & Electron Beam Technologies Research
Korea Institute of Machinery and Materials (KIMM)
Daejeon 34103, Republic of Korea

C. Kim
Memory Etch Technology Team
Samsung Electronics
Pyeongtaek-si 17786, Republic of Korea

The ORCID identification number(s) for the author(s) of this article can be found under https://doi.org/10.1002/aisy.202500517.

DOI: 10.1002/aisy.202500517

S. Kim
Department of Physics and Chemistry
Daegu Gyeongbuk Institute of Science and Technology (DGIST)
Daegu 42988, Republic of Korea

S. K. Jang
Electronic Convergence Material and Device Research Center
Korea Electronics Technology Institute (KETI)
Seongnam 13509, Republic of Korea

M. S. Bak
School of Mechanical Engineering
Sungkyunkwan University
Suwon 16419, Republic of Korea

W. S. Kang
Mechanical Engineering
KIMM Campus
University of Science & Technology (UST)
Daejeon 34113, Republic of Korea

J. Kim, J. Kim
Department of Mechanical and Design Engineering
Hongik University
Sejong 30016, Republic of Korea
E-mail: jk12@hongik.ac.kr

H.-U. Kim
Nano-Mechatronics
KIMM Campus
University of Science & Technology (UST)
Daejeon 34113, Republic of Korea

undercutting, leading to structural damage and degraded device yield.[8,9] Therefore, precise in situ monitoring of insulator thickness is essential for ensuring electrical performance and process control.

However, most etch process evaluations are performed via ex situ analysis after the wafers are transferred from the chamber following process completion.[10–13] This approach delays fabrication and increases contamination risk by exposing wafers to air and disrupting the chamber vacuum, affecting process reproducibility.[14,15] While in situ ellipsometry is widely used for etch depth monitoring, it involves long measurement times and is difficult to integrate into existing equipment.

Recently, digital image colorimetry (DIC) has gained attention for its noncontact, real-time capabilities and has been widely used in food science,[16–21] chemistry,[22–24] environmental sciences,[25] and biosciences,[26,27] as a convenient, cost-effective alternative to traditional methods without requiring expensive equipment. The integration of DIC with machine learning (ML) algorithms has been shown to enhance precision, enable automation, and support real-time predictions. Moreover, applying ML to DIC overcomes the limitations of conventional direct color-matching approach by enabling data-driven predictions.[28–30]

In this study, we propose a noncontact etch depth prediction method using red, green, and blue (RGB) data extracted via DIC, along with key process parameters. In plasma etching processes, acquiring nanometer-scale etch depth measurements is inherently challenging due to the limitations of in situ measurement and the limited available data samples.[31] To complement these limitations, recent advances in semiconductor modeling offer complementary perspectives to data-driven methods by capturing fundamental material behaviors.[32–37] An artificial neural network (ANN) is used to model the relationship between input data and etch depth, measured by ellipsometry as the output. In addition, we incorporate a Bayesian neural network (BNN) framework[38] to enable the estimation of prediction reliability.[39] This study shows that noncontact, DIC-based data can support etch depth prediction and broader process monitoring via ML, enabling noninvasive, in situ control that improves stability and yield in semiconductor manufacturing.

2. Experimental Section

In this study, ICP type reactive ion etcher (RIE; RAINBOW4420, Lam Research, Fremont, CA, USA) was used for plasma etching experiments. A high-density plasma was generated by applying radio frequency (RF) generator at 13.56 MHz to the top copper coil, while an additional RF generator was connected to the bottom electrode to regulate the DC bias voltage. Before the etching, the chamber was evacuated to a base pressure of 10^{-6} Torr using a turbomolecular pump (BOC Edwards, Burgess Hill, UK) to ensure a clean and stable environment. A precleaning process was carried out to remove residual contaminants by introducing a gas mixture of 50 sccm Ar and 20 sccm O_2, while applying 250 W to the top coil for 5 min.

Following the cleaning process, a coupon wafer ($1.5 \times 1.5\ cm^{-2}$, 300 nm SiO_2) was loaded into the chamber and the etching process was performed using a gas mixture of CF_4, O_2, and Ar. The flow rates of O_2 and Ar were fixed at 10 sccm, while the CF_4 flow rate was varied across four conditions, 5, 10, 15, and 20 sccm. The etching time was fixed at 180 s, and chamber pressure was varied across three levels: 20, 30, and 40 mTorr. The top power was varied from 50 to 110 W in 10 W increments, while the bottom power was maintained at 20 W. These experimental conditions resulted in a total of 84 conditions, summarized in **Table 1**. During the etching process, plasma characteristics were monitored in real-time using optical emission spectroscopy (OES; Maya2000Pro, Ocean Insight, Orlando, FL, USA). The OES system captures the intensity and wavelength variations of plasma emission, which reflect the interaction of reactants and by-products species during the etching process.[40,41] Spectral data were transmitted through an optical fiber positioned at the center of the view window.

Table 1. Process condition of ICP-RIE for SiO_2 etching.

Parameter	Unit	Conditions
Chamber pressure	mTorr	20, 30, 40
Plasma power (top)	W [watt]	50, 60, 70, 80, 90, 100, 110
Plasma power (bottom)	W [watt]	20
Process time	sec	180
Gas (CF_4)	sccm	5, 10, 15, 20
Gas (Ar)	sccm	10
Gas (O_2)	sccm	10

The etched SiO_2 samples were characterized using a spectroscopic ellipsometer (M-2000 V, J.A. Woollam, Lincoln, Nebraska,

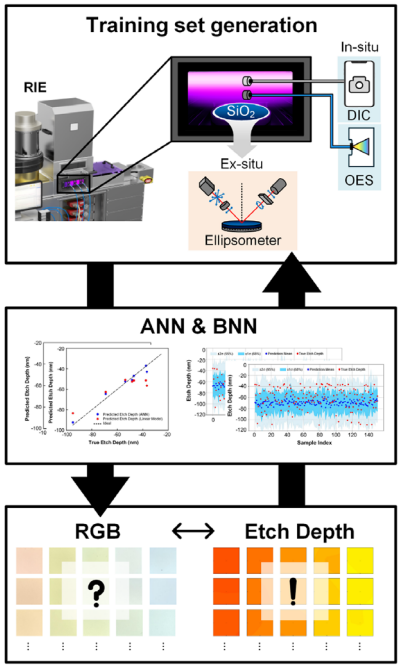

Figure 1. Schematic illustration of the etch depth prediction framework using in situ measurements and ML. During the RIE process, RGB data are collected via DIC, while plasma stability is monitored using in situ OES. These are paired with ellipsometer measurements of etch depth to train ANN and BNN models for predictive analysis.

USA) to confirm the thickness of SiO_2. Measurements were performed over an energy range of 1.0 to 3.5 eV, corresponding to wavelengths from 354 to 1240 nm. In addition, images for color analysis were captured using a smartphone camera (iPhone 12, Apple, Cupertino, CA, USA). To ensure consistent ambient lighting and photographic conditions, the coupon wafers were placed on a white background during image acquisition. Color data were extracted from a representative rectangular region on each sample. The red (R), green (G), and blue (B) colors ($0 \leq$ R, G, B $\leq$ 255) were quantified using the Image J software. **Figure 1** presents a schematic of the etch depth prediction framework, illustrating the overall workflow of data acquisition and model training. In this approach, in situ RGB data obtained from DIC is paired with ellipsometer measurements of etch depth. (Additionally, in situ OES data is utilized to verify plasma stability) These datasets are used to train ANN and BNN models for the purpose of predicting etch depth based on real-time, noncontact measurement.

3. Result and Discussion

3.1. Training Set Generation with Ex Situ Analysis

The results of the digital surface images are shown in **Figure 2**. The reference image, located at the top-right of Figure 2, corresponds to a 300 nm SiO_2 wafer. A distinct trend is observed in the etching behavior of SiO_2 under varying plasma conditions. As the top power increased from 50 to 110 W, the color of the etched samples becomes progressively lighter, indicating a higher etch rate. The effect of chamber pressure was also evident. At a pressure condition of 20 mTorr, samples exhibited more pronounced color changes compared to the other pressure conditions. In contrast, variations in the CF_4 flow rate showed minimal influence on surface color.

Figure 3 presents the ellipsometry measurements of SiO_2 thickness after etching under different top power, CF_4 flow rate, and chamber pressure conditions. The measured thickness trends aligned well with the digital surface image results: more extensive etching occurred at higher power levels and lower pressure. The color gradient represents the remaining SiO_2 thickness, with lighter shades indicating greater etch depth. A detailed thickness scale is provided in the top-right corner for reference and is consistently applied across all 84 conditions. The size and measured thickness of the reference sample are indicated in the middle-right section.

A distinct trend is observed, where higher top power and lower chamber pressure conditions result in enhanced etching performance. As the top power increases from 50 to 110 W, the remaining SiO_2 thickness decreases consistently across all pressure conditions. Similarly, lower chamber pressure (20 mTorr) leads to more pronounced etching compared to higher pressures. Specifically, under conditions of 20 W bottom power and 110 W top power, the average thickness decreased from 302.98 nm to 193.23 nm, confirming that the etching depth exceeded 100 nm. This phenomenon can be attributed to the increased mean free path of ions at lower pressures, which enhances their kinetic energy and leads to a more efficient etching process.[42] However, variations in CF_4 flow rate (5–20 sccm) had minimal impact on the etching behavior. This negligible

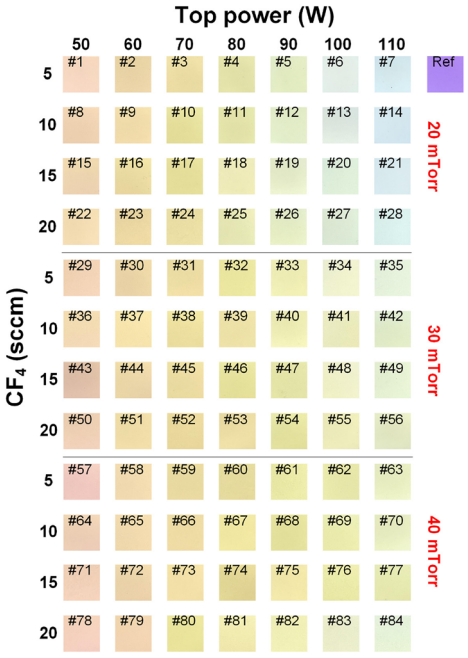

Figure 2. Digital surface images of SiO_2 coupon wafer (1.5 × 1.5 cm) captured by iPhone 12. A total of 84 images, including a reference sample, were acquired under varying chamber pressures (20, 30, and 40 mTorr) and CF_4 flow rates (5, 10, 15, and 20 sccm). The results are segmented by horizontal lines to distinguish different pressure conditions.

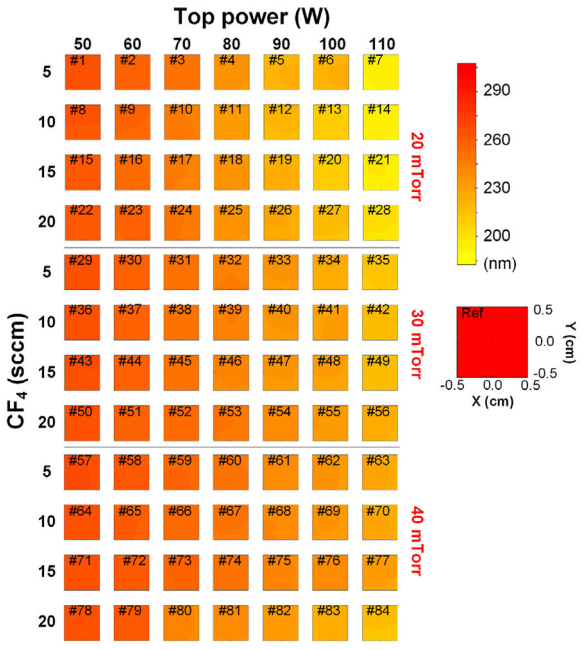

Figure 3. The thickness contour of SiO_2 coupon wafer (1.5 × 1.5 cm) by ellipsometry mapping with 9 points. A total of 84 measurements, including a reference sample, were performed under varying chamber pressures (20, 30, and 40 mTorr) and CF_4 volume flow rates (5, 10, 15, and 20 sccm). Horizontal lines are used to separate results by pressure conditions.

effect is attributed to the saturation of fluorine (F) radicals in the plasma, where an excess of CF_4 does not significantly increase the concentration active species participating in the etching reaction. Moreover, an excessive CF_4 flow may lead to the formation of carbon residues (CF_X), which can inhibit the etching process by depositing on the surface and reducing etch efficiency.[43,44]

3.2. In Situ Plasma Analysis

In our study, OES was used to verify plasma stability and indirectly detect abnormal process conditions. The results of the OES are shown in **Figure 4**. Upon initiating plasma discharge with a three-gas mixture, a series of spectral peaks was observed. Among these, Ar, O_2, and CF_3 were identified as key species expected to form during the etching process. Consequently, Ar ($\lambda = 750$ nm),[45] O_2 (630 nm),[46] and CF_3 (241.7 nm)[47] were monitored for analysis. All spectral data were normalized to compare analysis of intensity levels across different conditions. While minor fluctuations in peak intensities were intermittently observed, the overall emission patterns remained consistent. This consistency, though qualitative, supports the conclusion that the plasma was stable and the etching process proceeded under steady-state conditions.

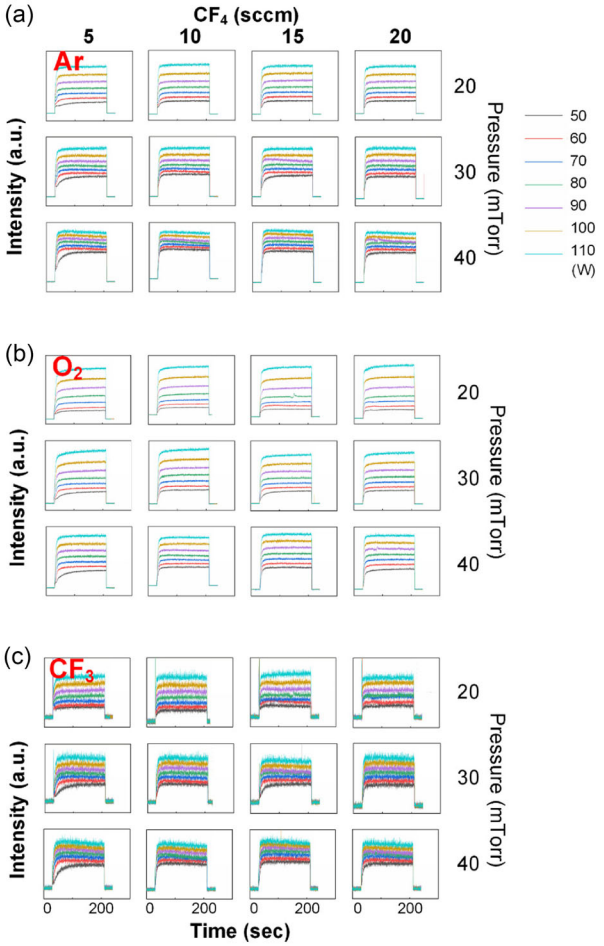

Figure 4. Normalized optical emission spectra a) Ar b) O_2 and c) CF_3, obtained under varying chamber pressures (20, 30, and 40 mTorr) and CF_4 flow rates (5, 10, 15, and 20 sccm). The emission profiles reflect stability of the plasma under process conditions, serving as indirect indicator of process steadiness.

3.3. Etch Depth Training with ML Models

To establish the relationship between the process parameters, we consider neural network models. A deep neural network is a hierarchical model in which each layer applies a linear transformation followed by a nonlinearity to the preceding layer. In brief, we consider an ANN which takes an n-dimensional vector $\boldsymbol{x}_0 \in R^n$ as an input, and outputs an m-dimensional vector $\boldsymbol{y} \in R^m$. If the ANN consists of k layers, the structure of the neural network is expressed as shown in Equation (1),

$$\boldsymbol{y}(\boldsymbol{x}_0; \{W^j\}, \{\boldsymbol{b}^j\}) = \psi_k W^k \psi_{k-1}(W^{k-1} \ldots \psi_2 \times (W^2 \psi_1(W^1 \boldsymbol{x}_0 + \boldsymbol{b}^1) + \boldsymbol{b}^2) + \boldsymbol{b}^{k-1}) + \boldsymbol{b}^k \quad (1)$$

where $W^j \in R^{d_j \times d_{j-1}}$ is a linear transformation $\boldsymbol{b}^j \in R^{d_j}$ is a bias, and $\psi_j : R^{d_j} \to R^{d_j}$ is an element-wise nonlinear activation function acting on each component of $(W^j \boldsymbol{x}_{j-1} + \boldsymbol{b}^j)$.

Given N training data points $\{\boldsymbol{x}_i, \boldsymbol{y}_i : i = 1, \ldots, N\}$, a user can optimize the weights W^j and biases $\boldsymbol{b}^j$ by defining a loss function L. For example, a typical choice for L is the mean squared error (MSE) as defined in Equation (2).

$$L(W^1, \ldots, W^k, \boldsymbol{b}^1, \ldots, \boldsymbol{b}^k) = \frac{1}{N} \sum_{i=1}^{N} (\boldsymbol{y}_i - \boldsymbol{y}_i)^2 \quad (2)$$

The problem of learning network weights is then formulated as the following optimization problem

$$\{W^1, \ldots, W_k, \boldsymbol{b}^1, \ldots, \boldsymbol{b}^k\} = \operatorname{argmin} L(\{W^j\}, \{\boldsymbol{b}^j\}) \quad (3)$$

A variety of computational techniques, including stochastic gradient descent and back-propagation, are available to solve the above problem. All neural network models used in this study are implemented using the PyTorch library.

Table 2 presents example datasets collected from the experiment. The input variables consist of three parameters: pressure (p), volume flow rate of CF_4 ($\dot{Q}_{CF_4}$), and RF plasma power (P) of the reactor. The output is SiO_2 wafer thickness (T) measured using an ellipsometer at nine different points. Based on the initial thickness information, the etched thickness can be readily calculated. Using the available dataset, we evaluate the potential of ANN models in two distinct scenarios.

3.3.1. Prediction of Etch Depth from Process Parameters

In the first scenario, we begin by predicting the average of nine measurements based on a given set of process parameters. In other words, $\boldsymbol{x}_0 = \{\mathrm{p},\ \dot{Q}_{CF_4},\ \mathrm{RF}\}$. To this end, 7 samples are randomly selected from the total 84 as a validation dataset, leaving 77 (=84-7) samples for training. This validation dataset is summarized in **Table 3**. Although the amount of data is limited, we aim to explore the potential of using an ANN to predict etching

Table 2. Example data set representing etched SiO_2 thickness.

p [mTorr]	$\dot{Q}_{CF4}$ [sccm]	RF P [W]	T. #1 [nm]	T. #2 [nm]	T. #3 [nm]	T. #4 [nm]	T. #5 [nm]	T. #6 [nm]	T. #7 [nm]	T.#8 [nm]	T.#9 [nm]
20	5	50	266.2	265.6	266.0	266.2	266.6	266.7	266.4	266.0	265.8
20	10	90	221.4	220.7	221.1	220.0	219.8	216.9	219.0	218.9	220.8
30	10	60	256.8	256.8	256.1	255.9	255.2	256.0	256.1	256.9	257.1
30	15	60	259.4	259.4	259.7	259.9	259.6	259.0	258.2	258.0	257.7
30	20	60	258.4	258.4	257.9	258.9	258.7	258.5	257.8	257.5	256.7

Table 3. Etch depth predictions from the ANN model (blue) from process parameters {p, $\dot{Q}_{CF_4}$, RF} compared to those from a linear model and the actual values. The MSE losses between the true values and the predictions from the ANN and linear models are 7.33 and 33.94, respectively.

p	$\dot{Q}_{CF4}$	RF P	True etch depth	Predicted etch depth (ANN)	Predicted etch depth (linear model)
40	15	80	−53.70	−57.13	−56.76
20	5	50	−36.80	−38.00	−38.65
40	5	70	−48.40	−48.70	−46.17
20	20	60	−47.00	−48.10	−49.98
20	10	100	−94.80	−93.90	−84.97
40	15	50	−37.60	−37.02	−29.41
20	10	80	−69.10	−66.84	−66.73

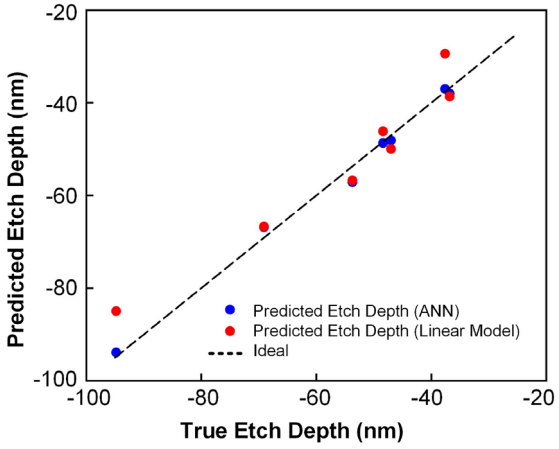

Figure 5. Etch depth predictions from the ANN model (blue), using process parameters {p, $\dot{Q}_{CF_4}$ P} compared to those from a linear model (orange) and the actual values (horizontal line).

performance. The neural network consists of an input layer with 3 features, a hidden layer with 32 neurons, and an output layer with a single neuron. The hidden layer applies a ReLU (rectified linear unit) activation function, introducing nonlinearity to improve learning capabilities. Additionally, a dropout layer with a probability of 20% is included, which randomly deactivates some neurons during training to prevent overfitting. The model is trained using the Adam optimizer with weight decay for regularization.

Next, to support the use of the ANN approach and evaluate its potentials in a more qualitative manner, we also construct a linear model

$$\boldsymbol{y}^l(\boldsymbol{x}_0; W^l, \boldsymbol{b}^l) = W^l \boldsymbol{x}_0 \tag{4}$$

and evaluate its error against the validation data. The result of validation test is summarized in Table 3 and **Figure 5**. The MSE losses between the true values and the predictions from the ANN and linear models are 7.33 and 33.94, respectively. The lower MSE of the ANN model justifies the use of this approach, as it accounts for nonlinear relationships between the process parameters and thickness.

Next, we extend the baseline predictive task by incorporating the variability present in the nine repeated measurements, with the goal of capturing both the uncertainty inherent in the data and the uncertainty in the model itself. Repeated measurements provide valuable information about data-level noise (aleatoric uncertainty), while a BNN can model uncertainty in the model parameters (epistemic uncertainty). By combining the two, one may obtain a more complete understanding of prediction reliability—especially important in semiconductor processes where both measurement error and model ambiguity are inevitable.

To retain the variability in repeated measurements, we treat each measurement as an individual data point rather than collapsing them into a mean value. This results in a dataset of 756 samples (9 measurements × 84 distinct process parameter combinations). Among these, 604 samples (≈80%) are used for training, and the remaining 152 for validation.

To model uncertainty and quantify predictive confidence, we use a BNN using the Monte Carlo (MC) Dropout technique. In this framework, model weights are implicitly treated as probabilistic by enabling dropout during both training and inference.[38] This allows the network to perform multiple stochastic forward passes for the same input, yielding a distribution of outputs that reflects model uncertainty. During inference, MC Dropout is performed by executing 50 stochastic forward passes for each validation input, thereby generating a distribution of predicted outputs. The mean of the sampled outputs is used as the final prediction, while the standard deviation represents the model's predictive uncertainty. To assess the model's reliability, the predicted uncertainty intervals are compared against the true etch depth values from the validation set.

A coverage analysis is performed to evaluate how often the true values fall within the predicted uncertainty intervals. Specifically, three categories are defined: (i) samples where the true value lies within the 1σ (68%) confidence interval, (ii) samples that lie outside the 1σ interval but within the 2σ (95%) interval, and (iii) samples that fall outside the 2σ interval. As visualized in **Figure 6**, 68.25% of the validation samples fall within the $\pm 1\sigma$ range, while an additional 23.81% lie within the $\pm 2\sigma$ range. Only 7.94% of the samples are outside the 2σ uncertainty bounds, indicating that the model successfully captures the variability of the data in most cases. These results indicate that the BNN effectively captures the underlying variability in the data and provides reliable uncertainty estimates. Such uncertainty quantification is especially valuable in semiconductor process modeling, where measurement noise and process fluctuations are inherent and critical to account for.

3.3.2. Prediction of Etch Depth from DIC

Next, we consider an ANN-based approach for predicting etching thickness from digital surface images. The underlying idea is that an ANN may be able to capture the relationship between the surface features shown in Figure 5 and the corresponding etching thickness illustrated in Figure 6. The primary motivation for exploring this relationship lies in the fact that acquiring digital surface images is significantly less costly than measuring actual thickness using an ellipsometer. Digital surface images were selected as a practical and cost-effective solution for real-time surface diagnostics. The use of digital imaging minimizes hardware modification and allows nonintrusive integration into existing process setups at minimal cost. Moreover, since this relationship is independent of specific plasma process parameters—such as p, $\dot{Q}_{CF_4}$, or RF power—the trained ANN model has the potential to generalize across different plasma processes, as shown in **Figure 7**.

Again, the number of ANN inputs is three, corresponding to the RGB channels of the digital surface images. Since the amount of training data is the same as in the previous case, we maintained the same neural network architecture. The model was trained using the Adam optimizer with weight decay applied for regularization. The results are summarized in **Table 4** and **Figure 8**, where the performance of the ANN is compared to that of a linear model. The MSE losses between the true values and the predictions from the ANN and linear models are 10.38 and 113.0, respectively. The substantially lower MSE of the ANN model compared to the linear model suggests that the relationship between RGB channels and etch thickness is more

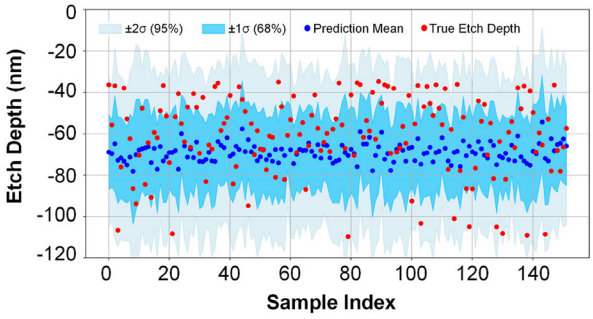

Figure 6. Prediction of etch depth with confidence intervals using the BNN model (blue dots) and actual etch depth values (red dots).

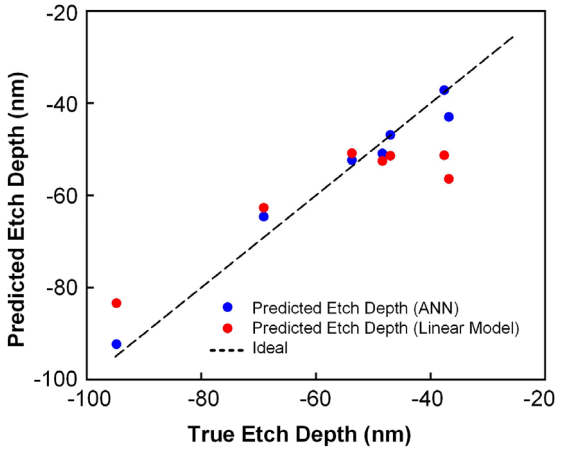

Figure 7. Etch depth predictions from the ANN model (blue) using RGB data of digital surface images compared to those from a linear model (red) and the actual values (horizontal line).

Table 4. Etch depth predictions from the ANN model (blue) from RGB data of digital surface images, compared to those from a linear model (orange) and the actual values (horizontal line). The MSE validation loss between the true values and the predictions from the ANN and linear models are 10.38 and 113.0, respectively.

R	G	B	True etch depth [nm]	ANN model prediction [nm]	Linear model prediction [nm]
228.8	151.2	216.3	−53.70	−52.38	−50.88
248.0	195.3	217.0	−36.80	−42.98	−56.46
234.0	159.9	218.9	−48.40	−50.94	−52.54
236.8	163.5	216.6	−47.00	−46.90	−51.41
224.2	225.3	235.1	−94.80	−92.33	−83.37
238.3	180.6	206.7	−37.60	−37.18	−51.32
227.2	170.1	228.4	−69.10	−64.62	−62.69

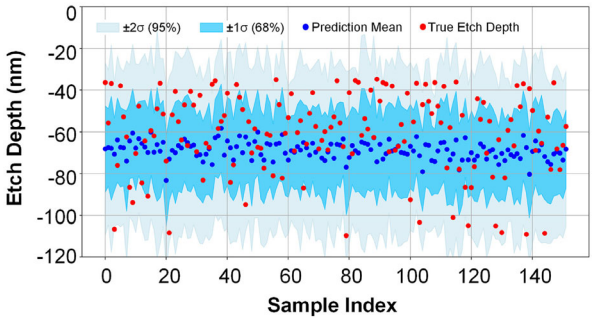

Figure 8. DIC prediction of etch depth and confidence intervals using the BNN model (blue dots) and actual etch depth values (red dots).

nonlinear than in previous cases, further justifying the use of the ANN-based approach.

Finally, we applied the same BNN approach using RGB digital surface inputs as model features. Each repeated RGB measurement was treated as an independent data point to preserve data-level variability, and MC Dropout was used to estimate predictive uncertainty through multiple stochastic forward passes.

A coverage analysis was conducted to assess the reliability of the model's uncertainty estimates. As illustrated in Figure 8, 63.16% of the validation samples fell within the $\pm 1\sigma$ (68%) confidence interval, and an additional 34.87% were within the $\pm 2\sigma$ (95%) range. Only 1.97% of the samples lay outside the $\pm 2\sigma$ bounds, indicating that the model successfully captured the variability present in the RGB data. These results confirm that the BNN framework provides robust uncertainty quantification even when using high-dimensional digital image features—an important capability for modeling semiconductor processes where both measurement noise and process variation are unavoidable.

4. Conclusion

This study introduces a noncontact, ML-based framework for in situ monitoring of etch depth in semiconductor manufacturing, offering a real-time and cost-effective alternative to conventional ex situ techniques. Two potential approaches were investigated. First, etch depth was predicted from process parameters using both ANN and BNN. The ANN effectively modeled the underlying nonlinear relationships, while the BNN facilitated uncertainty quantification, providing valuable insights into the confidence and robustness of the predictions.

In the second approach, RGB data from digital surface images were used as input features, demonstrating that reliable predictions can be achieved even in the absence of explicit process parameters. Notably, the BNN was capable of capturing both aleatoric and epistemic uncertainties, which is critical for high-precision applications.

The DIC with ML paves the way for advanced real-time diagnostics in plasma etching processes. By eliminating the need for chamber interruptions and reducing reliance on expensive metrology tools, the proposed framework enhances process stability and holds promise for improving device yield. Furthermore, the ability of BNNs to quantify prediction uncertainty provides a key advantage for decision-making in manufacturing environments where reliability and precision are paramount.

Acknowledgements

M.K. and S.K. contributed equally to this work. This work was supported by the Hongik University new faculty research support fund.

Conflict of Interest

The authors declare no conflict of interest.

Data Availability Statement

The data that support the findings of this study are available from the corresponding author upon reasonable request.

Keywords

artificial neural network, bayesian neural network, digital image colorimetry, plasma etching, prediction

Received: May 9, 2025
Revised: July 23, 2025
Published online: August 21, 2025

[1] M. F. Romero, M. M. Sanz, I. Tanarro, A. Jiménez, E. Muñoz, *J. Phys. D: Appl. Phys.* **2010**, *43*, 495202.
[2] H. H. Radamson, Y. Miao, Z. Zhou, Z. Wu, Z. Kong, J. Gao, H. Yang, Y. Ren, Y. Zhang, J. Shi, J. Xiang, H. Cui, B. Lu, J. Li, J. Liu, H. Lin, H. Xu, M. Li, J. Cao, C. He, *Nanomater.* **2024**, *14*, 837.
[3] Y. J. Jia, K. S. Kim, K. H. Kim, J. Y. Byun, G. Y. Yeom, *Appl. Sci. Converg. Technol.* **2019**, *28*, 142.
[4] S.-J. Tsai, C.-L. Wang, H.-C. Lee, C.-Y. Lin, J.-W. Chen, H.-W. Shiu, L.-Y. Chang, H.-T. Hsueh, H.-Y. Chen, J.-Y. Tsai, Y.-H. Lu, T.-C. Chang, L.-W. Tu, H. Teng, Y.-C. Chen, C.-H. Chen, C.-L. Wu, *Sci. Rep.* **2016**, *6*, 28326.
[5] K. Geng, D. Chen, Q. Zhou, H. Wang, *Electron.* **2018**, *7*, 416.
[6] S. Das, A. Sebastian, E. Pop, C. J. McClellan, A. D. Franklin, T. Grasser, T. Knobloch, Y. Illarionov, A. V. Penumatcha, J. Appenzeller, Z. Chen, W. Zhu, I. Asselberghs, L.-J. Li, U. E. Avci, N. Bhat, T. D. Anthopoulos, R. Singh, *Nat. Electron.* **2021**, *4*, 786.
[7] S. Yan, Z. Cong, N. Lu, J. Yue, Q. Luo, *Sci. China Inf. Sci.* **2023**, *66*, 200404.
[8] N. Lim, A. Efremov, K.-H. Kwon, *Thin Solid Films* **2019**, *685*, 97.
[9] R. J. Gasvoda, Z. Zhang, E. A. Hudson, S. Agarwal, *J. Vac. Sci. Technol. A.* **2021**, *39*, 040401.
[10] M. Huff, *Micromachines* **2021**, *12*, 991.
[11] D. Pasquariello, C. Hedlund, K. Hjort, *J. Electrochem. Soc.* **2000**, *147*, 2699.
[12] C. Kim, S. Lee, M. Kim, M. S. Choi, T. Kim, H.-U. Kim, *Appl. Sci. Converg. Technol.* **2023**, *32*, 106.
[13] C. Kim, M. Kim, D. Cho, C. K. Kanade, H. Seok, M. S. Bak, D. Kim, W. S. Kang, T. Kim, H.-U. Kim, *Chem. Mater.* **2023**, *35*, 1315.
[14] V. Dragoi, P. Lindner, *ECS Trans.* **2006**, *3*, 147.
[15] S. W. King, L. L. Smith, J. P. Barnak, J.-H. Ku, J. A. Christman, M. C. Benjamin, M. D. Bremser, R. J. Nemanich, R. F. Davis, *MRS Symp. Proc.* **2011**, *395*, 739.
[16] Y. Fan, J. Li, Y. Guo, L. Xie, G. Zhang, *Meas.* **2021**, *171*, 108829.
[17] K. Pounds, H. Bao, Y. Luo, J. De, K. Schneider, M. Correll, Z. Tong, *ACS Food Sci. Technol.* **2022**, *2*, 1309.
[18] B. V. Granados-Vega, C. Maldonado-Flores, C. S. Gómez-Navarro, W. M. Warren-Vega, A. Campos-Rodríguez, L. A. Romero-Cano, *Foods* **2023**, *12*, 3829.
[19] P. Masawat, A. Harfield, A. Namwong, *Food Chem.* **2015**, *184*, 23.
[20] J. Huang, J. Sun, A. R. Warden, X. Ding, *Food Control* **2020**, *108*, 106885.
[21] M. de Oliveira Krambeck Franco, W. T. Suarez, V. B. Dos Santos, *Food Anal. Methods.* **2017**, *10*, 508.
[22] M. D. Permana, L. K. Sakti, A. Luthfiah, M. L. Firdaus, T. Takei, D. R. Eddy, I. Rahayu, *Trends Sci.* **2023**, *20*, 5149.
[23] N. Bang-iam, Y. Udnan, P. Masawat, *Microchem. J.* **2013**, *106*, 270.

[24] Ö. F. Aydın, M. Aydın, M. Caliskan Demir, S. Kahraman, *Chemometr. Intell. Lab. Syst.* **2025**, *257*, 105310.
[25] M. L. Firdaus, W. Alwi, F. Trinoveldi, I. Rahayu, L. Rahmidar, K. Warsito, *Procedia Environ. Sci.* **2014**, *20*, 298.
[26] S. Bhatt, S. K. Singh, S. K. Datta, S. K. Dubey, *Proc. SPIE.* **2024**, *13008*, 1300803.
[27] W. Choi, J. Shin, K.-A. Hyun, J. Song, H.-I. Jung, *Biosens. Bioelectron.* **2019**, *130*, 414.
[28] S. Lee, Y. Park, P. Liu, M. Kim, H.-U. Kim, T. Kim, *Sensors* **2023**, *23*, 8226.
[29] M. Kang, S. K. Jang, J. Kim, S. Kim, C. Kim, H.-C. Lee, W. Kang, M. S. Choi, H. Kim, H.-U. Kim, *J. Sens. Actuator Netw.* **2024**, *13*, 75.
[30] Y. Park, P. Liu, S. Lee, J. Cho, E. Joo, H.-U. Kim, T. Kim, *Sensors* **2023**, *23*, 5563.
[31] A. Chernatynskiy, S. R. Phillpot, R. LeSar, *Annu. Rev. Mater. Res.* **2013**, *43*, 157.
[32] I. Abbas, T. Saeed, M. Alhothuali, *Silicon* **2021**, *13*, 1871.
[33] F. S. Alzahrani, I. A. Abbas, *Math.* **2020**, *8*, 585.
[34] E. Carrera, A. E. Abouelregal, I. A. Abbas, A. M. Zenkour, *Mech. Adv. Mater. Struct.* **2015**, *22*, 569.
[35] M. Marin, I. A. Abbas, R. Kumar, *Struct. Eng. & Mech.* **2014**, *51*, 651.
[36] M. I. Marin, R. P. Agarwal, I. A. Abbas, *Bound. Value Probl.* **2014**, *2014*, 129.
[37] A. Hobiny, I. Abbas, M. Marin, *Math.* **2022**, *10*, 121.
[38] Y. Gal, Z. Ghahramani, *Proc. Mach. Learn. Res.* **2016**, *48*, 1050.
[39] Y. Xue, S. Cheng, Y. Li, L. Tian, *Optica* **2019**, *6*, 618.
[40] A. Kolpaková, P. Kudrna, M. Tichý, *WDS'11 Proc. of Contributed Papers, Part II* **2011**, 180.
[41] B. Charles, K. J. Fredeen, *Concepts, Instrumentation And Techniques In Inductively Coupled Plasma Optical Emission Spectrometry* (3rd ed.). PerkinElmer Corp **1997**.
[42] M. A. Lieberman, A. J. Lichtenberg, *MRS Bull.* **2005**, *30*, 899.
[43] S.-X. Zhao, F. Gao, Y.-N. Wang, A. Bogaerts, *Plasma. Sources. Sci. T.* **2013**, *22*, 015017.
[44] J.-S. Jenq, J. Ding, J. W. Taylor, N. Hershkowitz, *Plasma. Sources. Sci. T.* **1994**, *3*, 154.
[45] F. P. Sainct, A. Durocher-Jean, R. K. Gangwar, N. Y. Mendoza Gonzalez, S. Coulombe, L. Stafford, *Plasma* **2020**, *3*, 38.
[46] W. Xu, X. Mao, N. Zhou, Q.-Y. Zhang, B. Peng, Y. Shen, *Vacuum* **2022**, *196*, 110785.
[47] M. Suto, N. Washida, *J. Chem. Phys.* **1983**, *78*, 1012.